Chemical Engineering Journal 411 (2021) 128383

Contents lists available at ScienceDirect

Chemical Engineering Journal

journal homepage: www.elsevier.com/locate/cej

Nanoparticle dynamics in the spatial afterglows of nonthermal plasma synthesis reactors

Xiaoshuang Chen [1], Christopher J. Hogan Jr. [*]

Department of Mechanical Engineering, University of Minnesota, Minneapolis, MN 55455, USA

ARTICLE INFO

Keywords:
Nanoparticle dynamics
Constant number Monte Carlo simulation
Nonthermal plasma synthesis
Spatial plasma afterglow

ABSTRACT

Nonthermal plasma flow tube reactors are industrially scalable systems for the production of nanocrystal (NC) based materials and coatings. One key advantage of nonthermal plasma synthesis is the ability to both synthesize NCs and deposit films in a single reactor, as at the reactor outlet, NCs can be inertially deposited onto a target substrate. The size and morphology of deposited particles can substantially influence the film structure and function. Though NCs are typically near-spherical and monodispersed as-produced in plasma synthesis reactors, NC charge and growth dynamics can be altered substantially when NCs are sampled out of the plasma and through the spatial afterglow region, affecting deposition. Experiments have demonstrated changes of NC size and charge in the spatial afterglow; however, these dynamics remain unexplored and unexplained via theory and simulation. To address this, we developed a constant number Monte Carlo (CNMC) simulation model to examine the mechanisms of NC decharging and growth in the spatial afterglow of plasma flow tube reactors. Collisions between NC and plasma species, diffusive deposition, and electron desorption from NCs are incorporated in the CNMC simulation. The simulation results are specifically compared with previous experiments on Si NCs synthesized from a low pressure Ar-SiH_4 nonthermal plasma reactor. The experiment-model comparison shows that CNMC models can be implemented which accurately model NC size distribution evolution in a spatial afterglow. Simultaneously, results show that improved collision models, energetic species diffusion models, and electron desorption models will be necessary to accurately depict NC dynamics in spatial afterglows.

1. Introduction

Nonthermal plasma synthesis flow tube reactors have become an essential tool in the synthesis of functional nanocrystals (NCs) [1–4]. The unique non-equilibrium environment of nonthermal plasmas, wherein the electron temperature is as high as several electronvolts but other plasma species are below 1000 K (or even at room temperature) enables the production of chemically-pure, size-controlled, low polydispersity NCs. In particular, the high electron energy in nonthermal plasmas can dissociate covalently bonded precursors to synthesize group 14 NCs, including but not limited to Si and Ge NCs, which are exceedingly difficult to produce with similar yields by alternative methods [1–3,5]. Other gas phase synthesis approaches, such as thermal pyrolysis of silanes in tube reactors generally require operating temperatures above 800 K, and the synthesis requires post-processing to modulate NC size [6,7]. Beyond facilitation of precursor dissociation, the disparate mobilities and masses of electrons and ions in plasmas further lead to an environment wherein nucleated NCs are unipolarly charged negative [8]; unipolar charging can mitigate NC-NC collisional growth (coagulation or aggregation). As surface growth processes tend to minimize NC polydispersity, nonthermal plasma reactors yield much more monodisperse NCs than all other vapor phase synthesis approaches.

The ability to produce NCs in nonthermal plasmas has facilitated development in a number of areas in nanotechnology, including but not limited to NC based semiconductor materials [9,10], NC based solar cells [11,12], catalyst production [13,14], and the application of NCs in bioimaging [15]. Plasma synthesized Si NCs, for example, have displayed rather extraordinary size tunable luminescence properties [16] with over 60% photoluminescence quantum yields [17], and have been applied in photoelectronic devices in a variety of ways [18–21]. Given the demonstrated scalability of plasma flow tube reactors and the unique non-equilibrium synthesis environment they provide, the areas of nanotechnology dependent upon plasma synthesized NCs are expected to continue to grow [2,3]. A particularly promising and growing set of applications of plasma synthesis depends not only on synthesized NC

* Corresponding author.
E-mail address: hogan108@umn.edu (C.J. Hogan).
[1] Present address: Department of Energy, Environmental & Chemical Engineering, Washington University in St. Louis, MO 63130, USA.

https://doi.org/10.1016/j.cej.2020.128383
Received 21 October 2020; Received in revised form 15 December 2020; Accepted 29 December 2020
Available online 4 January 2021
1385-8947/

Nomenclature

C_e	Electron number density
C_g	Gas molecule number density
C_{ion}	Ion number density
C_p	Nanocrystal number concentration
D_{tube}	Plasma tube reactor diameter
G_s^o	Electron solvation energy
H	Non-dimensional collision kernel
K_e	Electron mobility
Kn_D	Diffusive Knudsen number
K_p	Nanocrystal mobility
L_{eff}	Plasma characteristic length
M_{dep}	Mass of the nanocrystals deposited on the wall during a time step
M_k	Total nanocrystal mass in the simulation box at the beginning of kth time step
N	Number of nanocrystals in the simulation box
N_p	A nanocrystal in the simulation box.
$R_{dep,p}$	Nanocrystal wall deposition rate
$R_{dsp,p}$	Electron desorption rate
$R_{e,ion}$	Recombination rate
R_L	Maximum change of ion or electron density per unit time per unit density
R_T	Total number of events occurring per unit time
S_D	Non-dimensional screening length
T_e	Electron temperature
T_g	Gas temperature
T_{ion}	Ion temperature
T_p	Nanocrystal temperature
V_k	Simulation volume at kth time step
V_o	Primary nanocrystal volume
V_p	Aggregate nanocrystal volume
a_{ij}	Radii sum of two colliding species
a_p	Nanocrystal radius (spherical)
c_p	Nanocrystal bulk heat capacity
d_m	Nanocrystal mobility diameter
d_o	Primary nanocrystal diameter
d_p	Nanocrystal diameter (spherical)
e	Elementary charge
f_{ij}	Reduced friction factor
h	Planck's constant
k_B	Boltzmann constant
m_{ion}	Ion mass
m_{ij}	Reduced mass
m_p	Nanocrystal mass
n_m	Number of atoms in a single nanocrystal
r	A random number from uniform distribution between (0, 1)
t_k	Residence time of kth time step
Δt_k	Inter-event time in CNMC simulation at kth time step
v_g	Thermal velocity of the gas species
v_{ion}	Thermal velocity of ion
z_p	Number of elementary charges on the nanocrystal

Greek Letters

Δ	Electron desorption energy
Ψ_E	Potential energy ratio
α	Total number of events sampled in a time step
$\alpha_{dep,p}$	Number of nanocrystal deposition events in a time step
$\alpha_{dsp,p}$	Number of electron desorption events in a time step
$\alpha_{e,p}$	Number of electron-nanocrystal collision events in a time step
$\alpha_{g,p}$	Number of gas-nanocrystal collision events in a time step
α_{ij}	Number of nanocrystal-nanocrystal collision events in a time step
$\alpha_{ion,p}$	Number of ion-nanocrystal collision events in a time step
α_{po}	Number of events with reasonable possibility to happen in a time step
β	Collision kernel
$\beta_{e,ion}$	Electron-ion recombination kernel
$\beta_{e,p}$	Electron-nanocrystal collision kernel
$\beta_{g,p}$	Gas-nanocrystal collision kernel
β_{ij}	Nanocrystal-nanocrystal collision kernel
$\beta_{ion,p}$	Ion-nanocrystal collision kernel
ε	Relative permittivity
ε_0	Vacuum permittivity
η_C	Coulombic collision enhancement factor in the continuum regime
η_{FM}	Coulombic collision enhancement factor in the free molecular regime
λ_D	Debye length
λ_{ion}	Mean free path for ion-neutral collisions
ρ_g	Bulk density of the gas species

Other Characters

$\mathscr{D}_e$	Electron diffusion coefficient
$\mathscr{D}_{eff,e}$	Effective diffusion coefficient of electron
$\mathscr{D}_{eff,ion}$	Effective diffusion coefficient of ion
$\mathscr{D}_{ion}$	Ion diffusion coefficient
$\mathscr{D}_p$	Nanocrystal diffusion coefficient
$\mathscr{R}_0$	Rydberg unit of energy
$\mathbb{R}_i$	Reaction rate of a physical process

size and crystallinity, but also upon NC incorporation into thin films and 2D materials, with control over film microstructure and optoelectronic properties via control of process conditions [22–27]. Here, nonthermal plasma flow tube reactors have an additional advantage; synthesis and deposition to form films can be accomplished in a single reactor system without the need to transfer NCs out of solvent or to introduce a separate deposition system [22,24,28,29]. Instead, by passing NCs out of the plasma volume, and through a nozzle, film formation can be directly driven by inertial impaction [23,30].

However, the functional properties of plasma deposited materials strongly depend not only on the NC size and composition, but also on the sizes and morphologies of what objects are depositing, which are not necessarily isolated NCs. Studies have shown that the porosity of particulate films deposited from the gas phase increases if aggregated particles deposit [31,32] and that the film microstructure can affect electron transport dynamics in mesoporous films made of semiconductor NCs [33]. Control over deposition hence necessitates a fundamental understanding of not only primary NC nucleation and growth [34], but also post-plasma NC dynamics because NCs synthesized from nonthermal plasmas must be sampled out of the plasma reactor before depositing on any substrate. NC growth is not arrested upon exiting the plasma volume. Recent studies have reported that the charge state of NCs in the spatial afterglow, beyond the plasma volume, is orders of magnitude below the expected negative charge level of NCs in the plasma [35] and NCs can even become bipolarly charged in the afterglow [36–38]. Aggregation of NCs beyond the plasma volume has also been observed and quantified [38,39]; aggregation is presumably initiated due to neutralization and charge reversal of the NCs in the

spatial afterglow.

In the spatial plasma afterglow, the environment rapidly transforms from a non-equilibrium to an equilibrium state through a combination of ion-electron recombination, differential loss of electrons and ions to reactor walls, and decay of electron energies via electron-neutral collisions. Although NC decharging and aggregation in this environment have been observationally characterized via sampling NCs, in situ detection of NC charge reduction and subsequent aggregation is a challenge for current experimental methods, as the residence time of NCs in the spatial afterglow is usually as low as several milliseconds. Furthermore, in comparison to population balance modeling efforts in combustion and high temperature reacting flows [40–45], models accounting for NC interactions with energetic plasma species (ions and electrons) and monitoring NC collisional growth are much less commonplace (though with several noteworthy prior reports [46–48]). For this reason, nonthermal plasma synthesis and deposition systems are presently designed, modeled, and operated in a "black box" manner, and NC dynamics in spatial afterglows are incompletely understood. In an effort to address this issue, here we develop a constant number Monte Carlo (CNMC) [49,50] model to better study how unipolarly negative charged NCs synthesized in a nonthermal plasma flow tube volume can undergo decharging and charge reversal (i.e. how positively charged NCs result) and to better understand NC aggregation rates in post-plasma spatial afterglows. In the developed model, we uniquely account for the initial NC charge distribution in the plasma volume, and in the spatial afterglow we consider (1) NC-ion, NC-electron, ion-electron, and NC-NC collisions, (2) ion, electron, and NC convective losses to reactor walls, as well as (3) electron desorption from highly charged NCs, with the latter based on models of ion evaporation commonly used to examine highly charged droplets [51–53]. In modeling collisions between oppositely charged entities, we utilize recently developed rate coefficient expressions [54] which account for the influence of screening effects for particles present in plasma environments, as well as ion-neutral collisions across a wide collisionality regime. In modeling electron reactions, we account for the decay in electron temperature in the spatial afterglow [55] and consider both ambipolar [56] and free diffusion of plasma species. Finally, to model direct electron desorption (driven by the repulsive electrostatic energy in multiply charged NCs), we adapt the kinetic expressions proposed and experimentally verified by Fernandez de la Mora and coworkers [52,57,58] for ion evaporation from highly charged droplets. We specifically compare our simulation results with a recent experimental study of Si NCs synthesized via the decomposition of silane (SiH_4) in an Ar-SiH_4 flow-through low pressure nonthermal plasma reactor [38].

2. Constant number Monte Carlo simulation model in spatial afterglow

2.1. CNMC framework & initial conditions

In describing CNMC development, we refer to the case study measurements of Chen et al. [38] for initial conditions; these measurements correspond to the synthesis of Si NCs from a 2 Torr SiH_4-Ar plasma, with NC diameters below 10 nm. Though a specific case is examined in the

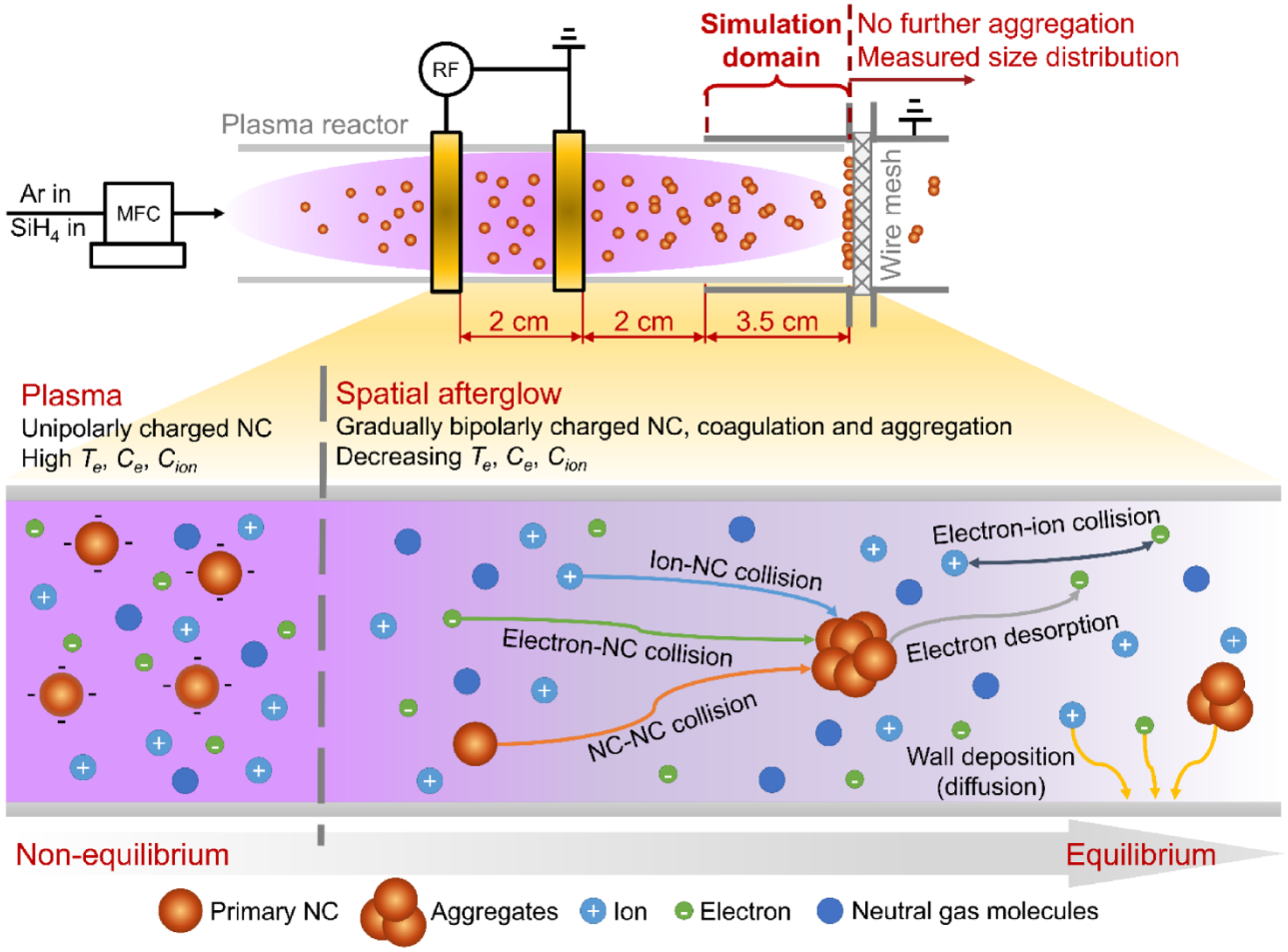

Fig. 1. A depiction of the processes that NCs and energetic species (electrons and ions) undergo as NCs leave plasma zone with illustration of the simulation domain compared with experiment by Chen et al [38]. In the studied experiment (upper image), primary Si NCs leaving the plasma reactor decharge and aggregate. Their concentrations are further reduced upon leaving the spatial afterglow via deposition on a wire mesh, quenching growth prior to ion mobility measurements.

present study, we note that the simulation procedure developed is general, and can be adapted to a wide variety of plasma synthesis reactors. An overview of the modelled reactor system and a depiction of the reactions NCs undergo in the plasma volume and spatial afterglow is depicted in Fig. 1. The upper depiction displays dimensions of the case study plasma reactor, where the spatial afterglow region downstream of the volume of the plasma reactor is the simulation domain. Within the volume of the reactor, elevated electron temperatures (T_e), electron densities (C_e), and ion densities (C_{ion}) persist, but because of the disparity in electron mobility and mass and ion mobility and mass, NCs are unipolarly negatively charged [8], and Coulombic repulsion effectively serves to mitigate NC-NC collisional growth [59]. However, as NCs are driven by flow to exit the plasma volume, the processes depicted in the lower "Spatial afterglow" region of Fig. 1 lead to a rapidly changing environment wherein the electron temperature decays to the background temperature, and NCs may decharge and agglomerate. Because of the diversity of rate processes occurring and the potential for the NC size distribution function to evolve, deterministic population balances, monitoring NC concentration evolution as a function of size and charge state, become prohibitively expensive. Meanwhile, Monte Carlo approaches can incorporate a diverse array of reactions, and require no assumption on the shapes of NC size and charge distributions [50,60–63].

In order to implement CNMC simulations [49,64] and simplify the numerical model of the NC dynamics in spatial afterglow, the following assumptions are made: 1) the temperatures of ions and NCs equilibrate with that of gas magnitude faster than the decay of electron temperature in the spatial afterglow, and can be treated as constants that equal to gas temperature throughout the simulation; 2) primary NCs and NC aggregates are approximated as spherical, with diameters determined by their masses and bulk densities; 3) ionization processes in the spatial afterglow are neglected; 4) electron temperature decay commences as soon as NC and energetic species flow into the simulation domain. In CNMC, the number of sample particles in the simulation box is constant, but the volume that the simulation box represents changes as particle number concentration changes due to coagulation or deposition. Each particle is represented by a specific number of atoms (yielding its diameter with a spherical-bulk density approximation) and has an integer charge level. To determine NC initial mass and charge states, we elect to first randomly sample $N = 10^4$ Si NC diameters from a normal distribution whose mean (6.8 nm) and standard deviation (1.5 nm) are based upon TEM measurements of primary NCs reported in Chen et al [38]. The initial charge state for each NC was determined from a smaller CNMC simulation considering electron-NC and ion-NC collisional charging reactions, electron desorption, and NC reaction induced heating and cooling (which affects the electron desorption rate) as described in Appendix A.

The initial plasma condition and primary NC conditions are listed in Table 1. The ion density and electron temperature are adapted from in plasma measurements by Mangolini and Kortshagen [65] from a similar plasma reactor of Si NC synthesis as that described in Chen et al [38]. The initial electron density C_e was calculated via the quasi-neutral requirement [2]:

$$C_e = C_{ion} + \overline{z_p} C_p \tag{1}$$

where $\overline{z_p} = \frac{\sum_{p=1}^{N} z_p}{N}$ is the average charge of primary NCs in the simulation box. The initial NC concentration C_p was calculated assuming 50% of the total input SiH_4 is converted to Si NCs that passed into the spatial afterglow with mean primary NC diameter $d_o = 6.8$nm. The remaining input precursors are believed to deposit on the reactor walls during synthesis. Mangolini et al [1] have quantified film deposition in such reactors, showing that the total film mass is consistent with 50% of the total mass input.

Table 1
Plasma and primary NC conditions in CNMC simulation and the corresponding experimental condition in Chen et al [38] used in model-experiment comparison.

Ion density [65]	5.0	$\times 10^{16}$ m^{-3}
Electron temperature [65]	4	eV
Plasma pressure [38]	2	Torr
Gas temperature	300	K
Primary NC mean diameter [38]	6.8	nm
Primary NC standard deviation [38]	1.5	nm
Primary NC concentration	3.26	$\times 10^{16}$ m^{-3}
SiH_4 flow rate	0.5	sccm
Ar flow rate	59.5	sccm
SiH_4 partial pressure	16.7	mTorr
Total flow rate	60	sccm
Plasma reactor I.D.	6.35	mm
Residence time in simulation domain	2.92	ms

2.2. Physical processes

A detailed flow chart of the CNMC simulation procedure is presented in Fig. 2. With CNMC, we calculate the occurrence of individual physical processes during an inter-event time Δt_k over successive time steps. At time step k the possibility that an event can happen is proportional to its reaction rate [49] provided the average time for reaction to occur is significantly larger than the time step selected. In the spatial afterglow, we consider the following physical, collisional, and chemical reactions, with their outcomes and rates noted:

1) Ion-NC collision, leading to charge transfer from the ion (Ar^+) to the NC. The NC charge z_p is changed by a +1 integer level when an ion collides with the NC:

$$z_p\big|^{k+1} = z_p\big|^{k} + 1 \tag{2}$$

The total number of ion-NC collisions $\alpha_{ion,p}$ across all NCs in the simulation box during inter-event time Δt_k at time step k can be calculated as:

$$\alpha_{ion,p} = \left(C_p C_{ion} \frac{\sum_{p=1}^{N} \beta_{ion,p}}{N} \right) V_k \Delta t_k \tag{3}$$

where $\beta_{ion,p}$ denotes the ion-NC collision kernel, V_k is the volume the simulation box represents at kth time step. Noting:

$$C_p = \frac{N}{V_k} \tag{4}$$

Eq. (3) can be simplified to:

$$\alpha_{ion,p} = C_{ion} \sum_{p=1}^{N} \beta_{ion,p} \Delta t_k \tag{5}$$

As described in detail in Appendix B, $\beta_{ion,p}$ is calculated accounting for screening influences using the model of Chahl & Gopalakrishnan [54], which has been shown to yield good agreement with charge distributions measured on nanoparticles in unipolar and bipolar environments [66,67] as well as molecular dynamics inferred ion-ion recombination rate coefficients [68]. This collision kernel expression depends upon the NC radius, ion mass, ion friction coefficient (linked to its mobility through the Stokes-Einstein relationship), and the background thermal energy.

2) Electron-NC collision, leading to binding of the electron to the NC. The NC charge is changed by an integer −1 when an electron collides with the NC:

$$z_p\big|^{k+1} = z_p\big|^{k} - 1 \tag{6}$$

Similar to the analysis for ion-NC collision, the total number of electron-NC collisions ($\alpha_{e,p}$) during time Δt_k is given as:

$$\alpha_{e,p} = C_e \sum_{p=1}^{N} \beta_{e,p} \Delta t_k \tag{7}$$

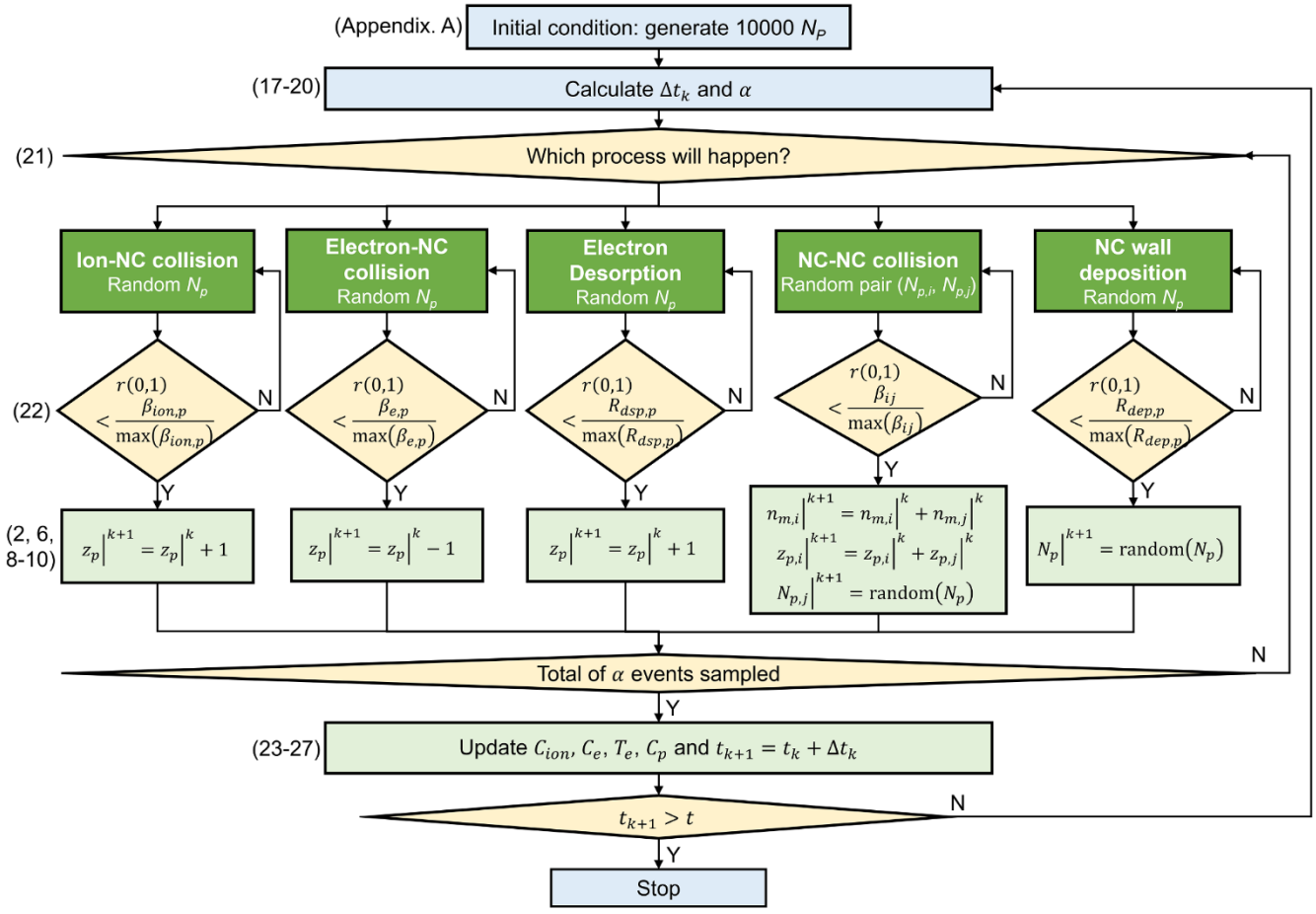

Fig. 2. Flow chart of the constant number Monte-Carlo simulation for the evolution of Si NC size and charge in a nonthermal plasma spatial afterglow. The number in the bracket to the left of the flow chart box denotes the equation number in the context.

where $\beta_{e,p}$ is the electron-NC collision kernel. The orbital motion limited model of electron-NC collisions is utilized to define $\beta_{e,p}$.[69,70]

3) NC-NC collision, occurring when two NCs $N_{p,i}$ and $N_{p,j}$ collide, a larger NC is formed (coagulation). In this instance, the size and charge state of i is updated with:

$$n_{m,i}|^{k+1} = n_{m,i}|^k + n_{m,j}|^k \tag{8}$$

$$z_{p,i}|^{k+1} = z_{p,i}|^k + z_{p,j}|^k \tag{9}$$

where n_m denotes the number of Si atoms in a NC. The vacancy at $N_{p,j}$ created in the simulation box after collision is filled by a randomly selected NC from the simulation box:

$$N_{p,j}|^{k+1} = \text{random}(N_p) \tag{10}$$

The total number of NC-NC collisions (α_{ij}) across all the pairs in the simulation box during time Δt_k is given by the equation:

$$\alpha_{ij} = \frac{C_p}{N}\sum_{i=1}^{N-1}\sum_{j=i+1}^{N}\beta_{ij}\Delta t_k \tag{11}$$

where β_{ij} is the NC-NC collision kernel. Again the collision model developed by Chahl and Gopalakrishnan [54] is used to calculate β_{ij}, as it can be adapted for collisions between similarly sized NCs, or NCs and ions.

4) Electron desorption from NCs, resulting in an integer charge increase by +1 as an electron is released from the NC. The change in NC properties during electron desorption is described by Eq. (2). The total number of electron desorption events $\alpha_{dsp,p}$ during the Δt_k interval is:

$$\alpha_{dsp,p} = \sum_{p=1}^{N} R_{dsp,p}\Delta t_k \tag{12}$$

where $R_{dsp,p}$ denotes desorption rate from a NC. Electron desorption from solid surfaces in plasmas and from highly charged particles has been discussed previously [53,71,72], with recent indirect experimental evidence for its occurrence [73]; however, an appropriate rate model has never been implemented for electron desorption in plasma flow tube reactors. We elect to adapt established ion desorption/evaporation models for multiply charged nanodroplets [52,74] to describe the electron desorption rate from spherical NCs. Using this approach, $R_{dsp,p}$ is given by the equation:

$$R_{dsp,p} = \frac{k_B T_p}{h}|z_p|\exp\left(-\frac{\Delta}{k_B T_p}\right) \tag{13}$$

where k_B is Boltzmann constant, T_p is NC temperature, h is Planck's constant, and Δ is the electron desorption energy. Following Gamero-Castaño and Fernandez de la Mora [57], Δ is defined as:

$$\Delta = G_s^o - \frac{e^2}{4\pi\varepsilon_0 a_p}\left[F(|z_p| - 1) + 4/5\right] \tag{14a}$$

where G_s^o is the "solvation" energy of the electron, ε_0 is the vacuum permittivity, e is the elementary charge, a_p is NC radius and $F(z)$ is a function decribed in [74]. The first part of Δ describes the maximum electron storage potential of a NC, and is composition dependent. The model of Bronold et al [53] estimates G_s^o as:

$$G_s^o = \frac{\mathscr{R}_0}{16}\left(\frac{\varepsilon-1}{\varepsilon+1}\right)^2 \tag{14b}$$

where $\mathscr{R}_0$ is the Rydberg unit of energy, and ε is the NC dielectric constant. Eq. (14b) yields 0.6 eV for Si, which is low in comparison to estimates of G_s^o made for a number of systems.[57,58] We hence raised G_s^o to 1 eV for comparison, which is more consistent in magnitude with the negative ion desorption barrier from highly charged liquid droplets [58]. The second term of Δ $\left(\frac{e^2}{4\pi\varepsilon_0 a_p}\left[F(z_p-1)+4/5\right]\right)$ accounts for the influence of surface curvature, and $R_{dsp,p}$ is hence strongly size dependant, i.e. the larger the NC radius the more charges it can contain. We compare results both including and excluding electron desorption (with the latter corresponding to $G_s^o = \infty$). In all instances $R_{dsp,p} = 0$ if $z_p = -1$.

5) NC convection to reactor walls, leading to loss of NCs. NCs depositing to the wall leave simulation box permanently and are replaced by a NC randomly selected from the simulation box, following Eq. (10). The deposited NC is recorded and accounted for in the change of NC concentration at the end of each time step. Similar to electron desorption, the total number of NC wall deposition events $\alpha_{dep,p}$ is calculated as:

$$\alpha_{dep,p} = \sum_{p=1}^{N} R_{dep,p}\Delta t_k \tag{15}$$

where $R_{dep,p}$ denotes the deposition rate. The Reynolds number for the case study reactor is ~14, and we utilize classical convective mass transfer models for laminar, fully developed internal flow [75] to calculate $R_{dep,p}$, i.e.:

$$R_{dep,p} = \frac{14.64\mathscr{D}_p}{D_{tube}^2} \tag{16}$$

where D_{tube} is the diameter of plasma tube reactor and $\mathscr{D}_p = \frac{3k_B T_g}{1.36\pi\rho_g v_g}\frac{1}{d_p^2}$ is NC diffusion coefficient, T_g is gas temperature, ρ_g is gas mass density, v_g is thermal velocity of the gas species and d_p is the NC diameter.

2.3. Calculation of inter-event time

To improve computational efficiency, multiple events are simulated in each time step. The size of the inter-event time Δt_k at time step k changes dynamically according to the event rates [49,76]:

$$\Delta t_k = \min\left(\frac{50}{R_T}, \frac{0.01}{R_L}\right) \tag{17}$$

where R_T is the total event rate. Combining Eqs. (5, 7, 11, 12, 15), yields:

$$R_T = \sum_{p=1}^{N}\left(C_{ion}\beta_{ion,p} + C_e\beta_{e,p} + R_{dsp,p} + R_{dep,p}\right) + \frac{C_p}{N}\sum_{i=1}^{N-1}\sum_{j=i+1}^{N}\beta_{ij} \tag{18}$$

R_L is the maximum change of ion or electron density per unit time per unit density. The change in ion and electron density is a result of diffusive deposition of the energetic species, electron-ion recombination, the collision of energetic species with NC and particularly for electron, electron desorption from NCs:

$$R_L = \max\left(\left|\frac{14.64\mathscr{D}_{eff,ion}}{D_{tube}^2} + \frac{R_{e,ion}}{C_{ion}} + \frac{C_p}{N}\sum_{p=1}^{N}\beta_{ion,p}\right|, \left|\frac{14.64\mathscr{D}_{eff,e}}{D_{tube}^2} + \frac{R_{e,ion}}{C_e} + \frac{C_p}{N}\sum_{p=1}^{N}\beta_{e,p} - \frac{C_p}{C_e}\frac{1}{N}\sum_{p=1}^{N}R_{dsp,p}\right|\right) \tag{19}$$

where $\mathscr{D}_{eff,ion}$ and $\mathscr{D}_{eff,e}$ are the effective diffusion coefficient of ions and electrons, respectively. We explore two separate models of diffusion for electrons and ions, free diffusion, and ambipolar diffusion. In the free diffusion model, the effective diffusion coefficient of electron $\mathscr{D}_{eff,e}$ and ion $\mathscr{D}_{eff,ion}$ equal the diffusion coefficient of the relative species calculated in isolation from one another, i.e. the electron diffusion coefficient $\mathscr{D}_e$ is calculated from electron mobility K_e from [77] using Einstein-Stokes equation $\mathscr{D}_e = \frac{k_B T_e}{e}K_e$, and the ion diffusion coefficient $\mathscr{D}_{ion} \cong \frac{v_{ion}\lambda_{ion}}{3}$ where v_{ion} is ion thermal velocity and λ_{ion} is mean free path for ion-neutral collision, noted in [78]. In the ambipolar diffusion model, $\mathscr{D}_{eff,e} = \mathscr{D}_{eff,ion} = \mathscr{D}_{ion}\left(1+\frac{T_e}{T_{ion}}\right)$, where T_{ion} is the ion temperature. In spatial afterglows, the system is expected to evolve from ambipolar diffusion at high energetic species densities, to free diffusion as energetic species decay [56]; however, without a clear model of this transition we elect to simply model these two limiting cases of energetic species deposition.

The same convection mass transfer model was applied to deposition of NC and energetic species [75]. $R_{e,ion} = C_e C_{ion}\beta_{e,ion}$ is the number of electron-ion collisions per unit time per unit volume (recombination); $\beta_{e,ion}$ is the electron-ion recombination kernel, calculated using the orbital motion limited approach [69,70]. The inter-event time Δt_k at time step k is chosen such that 50 total events can happen within the time interval or 1% maximum change in ion and electron density occurs, whichever leads to the smaller time interval. To reduce computation time, the change rate of C_{ion} or C_e is not considered if C_{ion} or C_e is less than 10^{-4} of the NC concentration. The total number of events α in the selected inter-event time is hence:

$$\alpha = \begin{cases} 50, & if\ \frac{50}{R_T} \le \frac{0.01}{R_L} \\ Poisson(R_T\Delta t_k), & if\ \frac{50}{R_T} > \frac{0.01}{R_L} \end{cases} \tag{20}$$

If $\frac{50}{R_T} > \frac{0.01}{R_L}$, α is sampled randomly from a Poisson distribution with an expectation of $R_T\Delta t_k$. Occasionally, the reaction rate of one or several dominating events can be magnitudes higher than all the others and results in $R_T \approx \sum_d R(N_p)$, where the subscript "$d$" indicates dominating events. In these instances, if the total number of these dominating events is lower than α from Eq. (20), the simulation algorithm leads to a continuous search for events that are extremely rare, after the dominant events are executed. To avoid this scenario, we additionally estimate the total number of potential events that have a reasonable possibility to happen in current time step α_{po}, with the criteria $\frac{\mathbb{R}_i}{\sum_{i=1}^{5}\mathbb{R}_i} > 0.05$ and $\frac{\beta(N_p)}{max(\beta)}$ *or* $\frac{R(N_p)}{max(R)} > 0.01$ (defined subsequently in Eqs. 21–22). If $\alpha_{po} < \alpha$, $\alpha = \alpha_{po}$, and the inter-event time is adjusted to $\Delta t_k = \frac{\alpha_{po}}{R_T}$.

2.4. Simulation of physical processes

With calculated Δt_k and α, CNMC time steps are executed through decision of which physical events will happen and on which NC or NC pairs. The probability that one of 5 physical processes can happen among α events is proportional to the process's combined reaction rates. Process n can happen if a random number r between (0, 1) follows:

$$\frac{\sum_{i=1}^{n-1}\mathbb{R}_i}{\sum_{i=1}^{5}\mathbb{R}_i} < r < \frac{\sum_{i=1}^{n}\mathbb{R}_i}{\sum_{i=1}^{5}\mathbb{R}_i} \tag{21}$$

where $\mathbb{R}_i$ denotes the reaction rate of a physical process; for ion-NC collision $\mathbb{R}_i = \sum_{p=1}^{N} C_{ion}\beta_{ion,p}$, for electron-NC collision $\mathbb{R}_i = \sum_{p=1}^{N} C_e\beta_{e,p}$, for NC-NC collision $\mathbb{R}_i = \frac{C_p}{N}\sum_{i=1}^{N-1}\sum_{j=i+1}^{N}\beta_{ij}$, for electron desorption $\mathbb{R}_i = \sum_{p=1}^{N} R_{dsp,p}$, for NC deposition to the wall $\mathbb{R}_i = \sum_{p=1}^{N} R_{dep,p}$.

After identifying the physical process which occurs, to find the NC or NCs that will experience the selected physical event, a new random number r between (0, 1) is generated. A NC (N_p) is randomly selected from the simulation box iteratively until the following condition is satisfied:

$$r < \begin{cases} \dfrac{\beta(N_p)}{max(\beta)}, & \text{for } \beta_{ion,p} \text{ and } \beta_{e,p} \\ \dfrac{\beta(N_{p,i}, N_{p,j})}{max(\beta)}, & \text{for } \beta_{ij} \\ \dfrac{R(N_p)}{max(R)}, & \text{for } R_{dsp,p} \text{ and } R_{dep,p} \end{cases} \quad (22)$$

The expressions employed in Eq. (22) depend upon the physical process that is selected by Eq. (21). The properties of N_p are updated following Eqs. (2, 6, 8–10) accordingly after selection of α events. Each NC is only allowed to experience one physical event in a time step. Subsequently, the electron and ion densities C_e and C_{ion} are updated for the next time step:

$$C_{ion}|^{k+1} = C_{ion}|^{k} - \Delta t_k \left(\frac{14.64 \mathscr{D}_{eff,ion}}{D_{tube}^2} C_{ion}|^{k} + R_{e,ion} + C_p|^{k} \frac{\alpha_{ion,p}}{N \Delta t_k} \right) \quad (23)$$

$$C_e|^{k+1} = C_e|^{k} - \Delta t_k \left(\frac{14.64 \mathscr{D}_{eff,e}}{D_{tube}^2} C_e|^{k} + R_{e,ion} + C_p|^{k} \frac{\alpha_{e,p} - \alpha_{dsp,p}}{N \Delta t_k} \right) \quad (24)$$

where $\alpha_{ion,p}$, $\alpha_{e,p}$, $\alpha_{dsp,p}$ are actual number of ion-NC collisions, electron-NC collisions and electron desorption events simulated in the time step k. NC concentration C_p is updated based upon mass conservation, accounting for aggregation and deposition:

$$C_p|^{k+1} = C_p|^{k} \frac{M_k - M_{dep}}{M_{k+1}} \quad (25)$$

where M_k is the total NC mass in the simulation box at the beginning of kth time step, M_{dep} is the mass of the NCs deposited on the wall during kth time step. As there is no available model for electron temperature decay in spatial afterglows, we implemented the global model of a temporal afterglow [55,79] to simulate the electron temperature T_e decay:

$$T_e|^{k+1} = \frac{T_e|^{0}}{\left(1 + 2t_{k+1}\sqrt{eT_e|^{0}/m_{ion}}/L_{eff}\right)^2} \quad (26)$$

where $T_e|^0$ is the initial electron temperature, m_{ion} is ion mass and L_{eff} is plasma characteristic length, here $L_{eff} = 0.02$m. t_{k+1} is the residence time of $(k+1)$th time step:

$$t_{k+1} = t_k + \Delta t_k \quad (27)$$

The procedure described in Eqs. (2)–(27) continues iteratively time step by time step. The CNMC simulation stopped when the residence time in simulation t_{k+1} reached a pre-set time t. Validation of the entire approach through comparison to the evolution of average NC mass considering collisional growth is provided in the fully collisional limit in the Supplementary material [80].

3. Results and discussion

3.1. Numerical analysis of nanocrystal dynamics in spatial afterglow

Comparison of CNMC results to measurements does require proper consideration of how NCs and NC aggregates were characterized, which was via ion mobility spectrometry (IMS) in Chen et al [38]. First, in an IMS measurement of NCs at sub-atmospheric pressure, the mobility (K_p) of a charged entity is linked to its mobility diameter (d_m) via the equation [81]:

$$K_p = \frac{3 z_p e}{1.36 \pi \rho_g v_g} \frac{1}{{d_m}^2} \quad (28)$$

For non-spherical aggregates, most studies suggest that the mobility diameter, d_m, is a projected area equivalent diameter [82–84]. CNMC results yield the volumetric aggregate size distribution, as opposed to projected areas. Using TEM measurements, Chen et al [38], provide a link between NC aggregate normalized volume and projected area based mobility diameter. Fitting to their results (Fig. 3a) yields:

$$d_m = 1.261 d_o \left(V_p/V_o\right)^{0.432} \quad (29)$$

where primary NC diameter $d_o = 6.8$nm, V_p is the volume of an Si NC aggregate and V_o is the primary NC volume (assumed spherical). The normalized NC aggregate volume V_p/V_o also reflects the number of primary NCs in an aggregate. We utilize Eq. (29) to calculate the mobility diameter of NC aggregates and to compare CNMC results to measurements. While the non-spherical nature of aggregates is not considered in aggregate-aggregate collisional growth or ionization in CNMC, we remark that for small aggregates (fewer than 50 primary NCs, as observed in experiments), preliminary calculations (not shown) suggested the effect of aggregate morphology on rates does not strongly affect the presented comparison.

A second important point in experiments is that the detection efficiency of NCs and NC aggregates was likely size dependent. The detector of the IMS system employed in Chen et al was a Faraday cage electrometer where NCs and NC aggregates needed to deposit by inertial impaction, and NCs smaller than an undetermined critical size were not detected efficiently. Furthermore, a wire mesh was implemented prior to IMS measurements to collect NCs and reduce their concentration, this was necessary to reduce further aggregation in sampling lines (i.e. to mitigate measurement-induced aggregation) as demonstrated, by Chen et al [36]. Wire meshes will efficiently collect smaller NCs via diffusive deposition [85]. Thirdly, as shown subsequently, CNMC simulations suggest that at the point of measurement, there would be an appreciable number of primary NCs remaining, but this was not observed in measurement (TEM observed NCs were largely aggregated). We therefore proceed with comparison using Eq. (29), and only plotting results for NC aggregates, i.e. we assume that prior IMS measurements were inefficient in the detection of primary NCs in comparison to aggregate detection, an assumption which requires scrutiny in future work with improved measurement schemes and models.

Fig. 3(b) displays a plot of the fraction of CNMC simulated NCs which are aggregates (composed of more than one primary NC) as a function of simulation time. As shown in Appendix B, initially, NCs are negatively charged as they leave the plasma reactor (except for the smallest NCs with the lowest simulated solvation energy). The increasing number of aggregates with time for all simulated conditions demonstrates that irrespective of electron desorption kinetics and energetic species deposition kinetics, NCs decharge in the spatial afterglow and then hence growth via NC-NC growth, in line with experimental observations. Fig. 3 (c) displays a plot of the ratio of +1 to −1 charged NCs as a function of time within the spatial afterglow for all six model parameter combinations tested. Experimentally, NC aggregates in the sub-20 nm size range have been found to be largely neutral or bipolarly singly charged (either +1 or −1 charge states) after passing through spatial afterglows, with +1 and −1 NC charge state concentrations similar in magnitude to one another in both the experimental case study [38] examined here and in atmospheric pressure nonthermal plasma reactors [37]. In Fig. 3(b-c) an arrow and vertical line denote respectively the experimentally estimated residence time within the spatial afterglow. As per Fig. 3(c), there is a stark difference in the ratio of +1/−1 charge state NC aggregates predicted by CNMC simulations with free diffusion and ambipolar diffusion of energetic species. The free diffusion models, specifically in the absence of electron desorption find best agreement with the experimentally observed ratio near 10^0, hence it is not necessary for electron desorption to explain prior IMS measurements.

Fig. 3(d-f) display comparisons of NC aggregate mobility diameter distributions from CNMC (which are only a minority of the total simulated NCs, as per Fig. 3b) to experimental measurements combining all

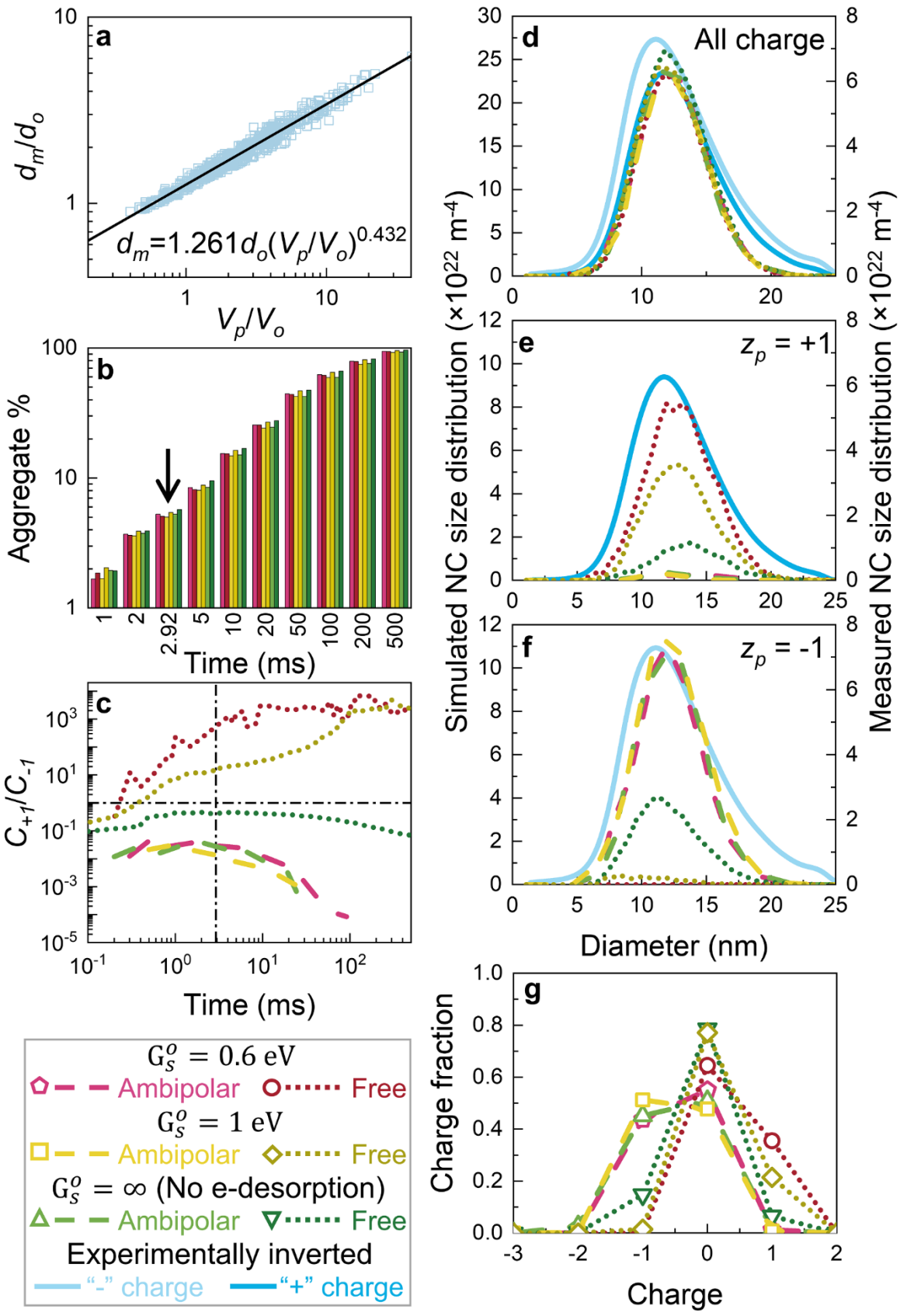

(caption on next page)

Fig. 3. Comparison between experiment [38] and CNMC results. (a) The mobility diameter d_m of Si NCs dimensionalized by primary NC mean diameter d_o from TEM image analysis of Chen et al [38] as a function of normalized NC volume V_p/V_o. The fit equation (solid line) is used to convert NC volume to mobility diameter to compare simulations to experiments for aggregates. (b) The percent of aggregates (composed of more than one primary NC) in the simulation box and (c) the concentration ratio of + 1 to −1 charge state aggregates as a function of NC residence time in spatial afterglow. The horizontal black dash-dot line in (c) is the unity ratio to guide the eye. The arrow in (b) and vertical black dash-dot line in (c) corresponds to the distribution snapshots in (d-g). (d-g) Simulation results of NC aggregate size distribution for (d) all charge states, (e) the +1 charge state and (f) the −1 charge state, and (g) NC aggregate charge fractions at the condition listed in Table 1. Results are compared with experimental results by Chen et al [38] for positively and negatively charged NCs. The CNMC models utilized incorporate low (0.6 eV) electron solvation energy, high (1 eV) electron solvation energy, and exclude electron desorption, and utilize either ambipolar or free diffusion to determine the wall deposition of energetic species.

charge states, as well as the +1 and −1 charge states, which are distinguishable in experiments. To our knowledge, this is the first attempt to compare gas phase aggregation and growth models to online measured NC size distributions in low pressure, non-thermal plasma reactors. All distributions from simulations are smoothed with a built-in smooth function in MATLAB with a 5-point moving average. Additionally, Fig. 3(g) plots the number averaged charge fractions in simulations for NC aggregates. While certainly multiple assumptions go into this comparison, the CNMC results in Fig. 3(d-f) are in good agreement with experimental measurements, suggesting experimental IMS observations were biased towards aggregates and that aggregation is facilitated by decharging due to differential loss of electrons and ions (and possibly direct electron desorption), leading to an ion-rich environment where charge reversal and aggregation can occur. These results also support the application of CNMC approaches as a means to evaluate NC dynamics in spatial plasma afterglow environments. At the same time, although both positively and negatively charged NC size distribution can be visibly observed in Fig. 3(d-f) and a bipolar charge distribution is evident in Fig. 3(g) when free diffusion model is applied and electron desorption is excluded, we find that even in this case the resulted positively charged NC concentration is still nearly 2 times lower than that of negative NCs. As shown in Fig. 3(c), positively charged NC concentrations approaching and exceeding negatively charged NC concentrations only results if the electron desorption mechanism is considered and if a free diffusion model is applied to electrons and ions. However, the free diffusion model and the inclusion of the electron desorption model lead to vanishingly small concentrations of negatively charged NCs, which is inconsistent with experiments. Therefore, results suggest further refinements of the rate expressions governing NC dynamics in spatial afterglows are needed for more accurate model predictions. As examples, as neither ambipolar nor free diffusion models fully describe experimentally observed NC charge distributions, it is likely that a transition from ambipolar to free diffusion for energetic species in the spatial afterglow occurs, and needs to be accounted for. The electron temperature decay model employed was developed from measurements of temporal afterglows [55], and does not account for how electron-NC collisions influence the electron energy distribution function. A coupled electron energy, electron-NC collision model may yield more accurate predictions of NC charge distribution evolution. Furthermore, improved NC-NC collision rate expressions, accounting for charged-neutral potential interactions [86,87] may lead to more accurate predictions of NC aggregate growth rates.

3.2. CNMC visualization of physical processes in the spatial afterglow

While measurement-model comparison is imperfect, because the CNMC model accounts for a diverse array of processes, it is informative to examine the occurrences of each reaction considered for the simulations which result in the Fig. 3 displayed size distributions. Fig. 4(a-f) display the cumulate occurrences of each examined process in 0.5 s of residence time, while Figs. 4(g-l) and 5 display the relative occurrence frequencies of all reactions (expressed as a percentage of the total events) as functions of residence time, separating processes involving NCs (Fig. 4), and those only involving energetic species (Fig. 5). Also plotted in the area plots are the NC mass and number concentrations, as well as the modeled electron temperature and ion and electron densities.

These plots are collectively of utility in examining temporal changes in dynamics in the spatial afterglow, and how changes to energetic species diffusivity and consideration of electron desorption influence NC dynamics. Beginning with instances implementing ambipolar diffusion, ion-NC, electron-NC, and electron desorption (when it is considered) occur at the earliest simulation times. These processes are a continuation of the physical dynamics in plasma volume, where ion-NC collisions and electron desorption balance with electron-NC collisions. As electron temperature decreases in the spatial afterglow, the electron-NC collision rate decreases, and ion-NC collisions start to dominate. The low solvation energy case has the most electron desorption occurrences in 0.5 s, as shown in Fig. 4(a), and for the conditions in Fig. 4(g) in the initial simulation stage (at smaller times than depicted) the occurrence frequency of electron desorption is equivalent to the electron-NC collision frequency. With ambipolar diffusion, charged species densities remain relatively constant until the 10^{-1} μs period; at this time ion and electron densities begin to decay at similar rates. NC-NC collision and NC deposition subsequently are prevalent at times beyond 100 μs. However, in this instance, as ions are depleted, there are insufficient ion-NC collisions to form positively charged NCs.

In many respects, free diffusion provides a similar picture to the ambipolar model, but electron densities begin to decay at 10^{-3} μs, leaving an ion rich environment to promote faster NC decharging via ion-NC collisions. Consequently, this leads to faster NC-NC aggregation, and the formation of positively charged NCs via ion-NC collision without the opportunity for electron-NC reverse collision. However, in the absence of electron desorption, initially, NCs are much more highly negatively charged (Fig. A.1) and while ion-NC collision serves on reducing the negative charge on NCs, the ion density depletes prior to the charge reversal of NCs.

3.3. Influence of process parameters on NC dynamics

The processing parameters in NC synthesis reactors, i.e. flow residence time and precursor number concentration, are important parameters in tuning the size and morphology of synthesized NCs. The experiments in Chen et al [38] show clearly that the aggregate size increases with SiH_4 partial pressure but is insensitive to residence time, which is distinct from atmospheric pressure growth systems [39]. Typically, longer residence time leads to larger aggregates because it provides additional time for aggregation. We additionally employ CNMC analysis to determine if the applied rate expressions for charging and decharging, deposition, and aggregation are consistent with experimental measurements with variable precursor concentration.

As experimentally observed primary NC sizes are only weakly correlated with NC aggregate size, we elect to investigate the influence of processing parameters utilizing the same initial primary NC size distributions as in the aforementioned simulations. Fig. 6 displays comparisons of measurement-inferred- and CNMC-predicted-NC aggregate mobility diameter and number concentration evolution, at varying precursor number concentration (with assumed 50% conversion to NCs). The displayed model results are obtained with the low electron solvation energy (0.6 eV which result in the highest electron desorption rate) and the free diffusion models. CNMC results for other simulation input conditions and for all NCs in the simulation box (both primary NCs and aggregates) are provided in Fig. S.1. CNMC results agree well with

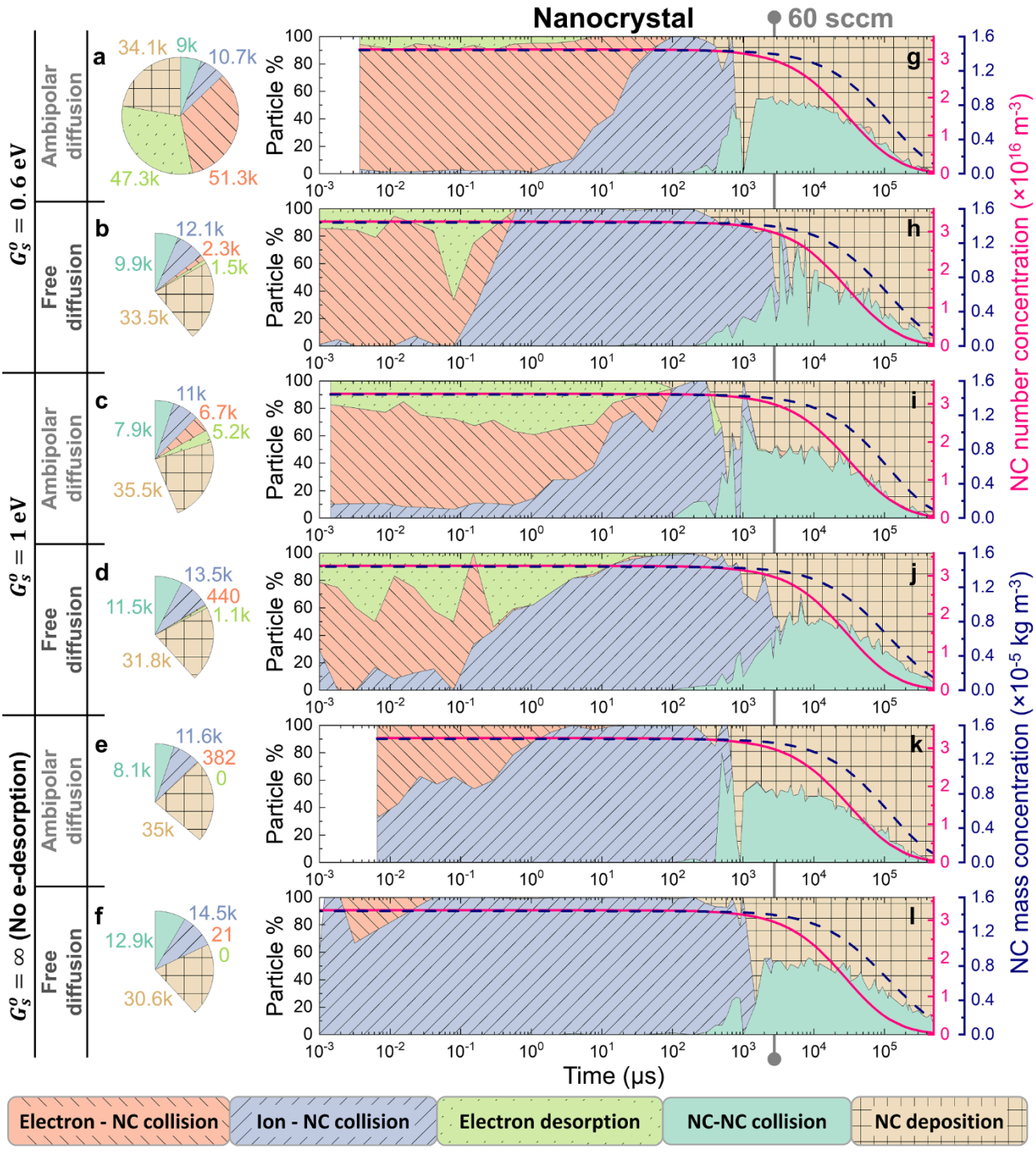

Fig. 4. NC dynamics from CNMC simulation. (a-f) Pie charts depicting the cumulative occurrence of physical events NCs experience in 0.5 s residence time with area relative to the total cumulative events for 0.6 eV solvation energy and the ambipolar diffusion model. (g-r) Area plots showing the percent occurrences of different reaction processes as a function of NC residence time in the spatial afterglow. The line plots are the changes in the NC total number and total mass concentration with respect to residence time indicated by the color of right ordinate. The CNMC simulation models and conditions are same as those utilized in Fig. 3. The grey solid line connecting plots indicates the residence time of NCs in the spatial afterglow of the examined experiment [38].

experimental measurements both of mean NC mobility diameter and concentration; the latter was determined from experimental measurements via integration of inverted size distributions and agreement observed between measurements and model results is obtained without any adjustments (aside from exclusion of primary NCs). The agreement in the concentration magnitudes of aggregates in simulation and detected NC in experiment again suggests that the majority of primary NCs were not transmitted through the detection system in the experiment. CNMC simulations with variable precursor concentrations reveal that (1) charged NC aggregates are generally larger than the neutral NCs, as larger NC aggregates are more likely to collide with energetic species, (2) the aggregate number concentration first increases when primary NCs collide to form aggregates and then decreases due to growth of the aggregates and wall deposition, and (3) larger NC aggregates are formed with higher precursor concentrations (Fig. 6a-d), which is in excellent agreement with experiments. At the same time,

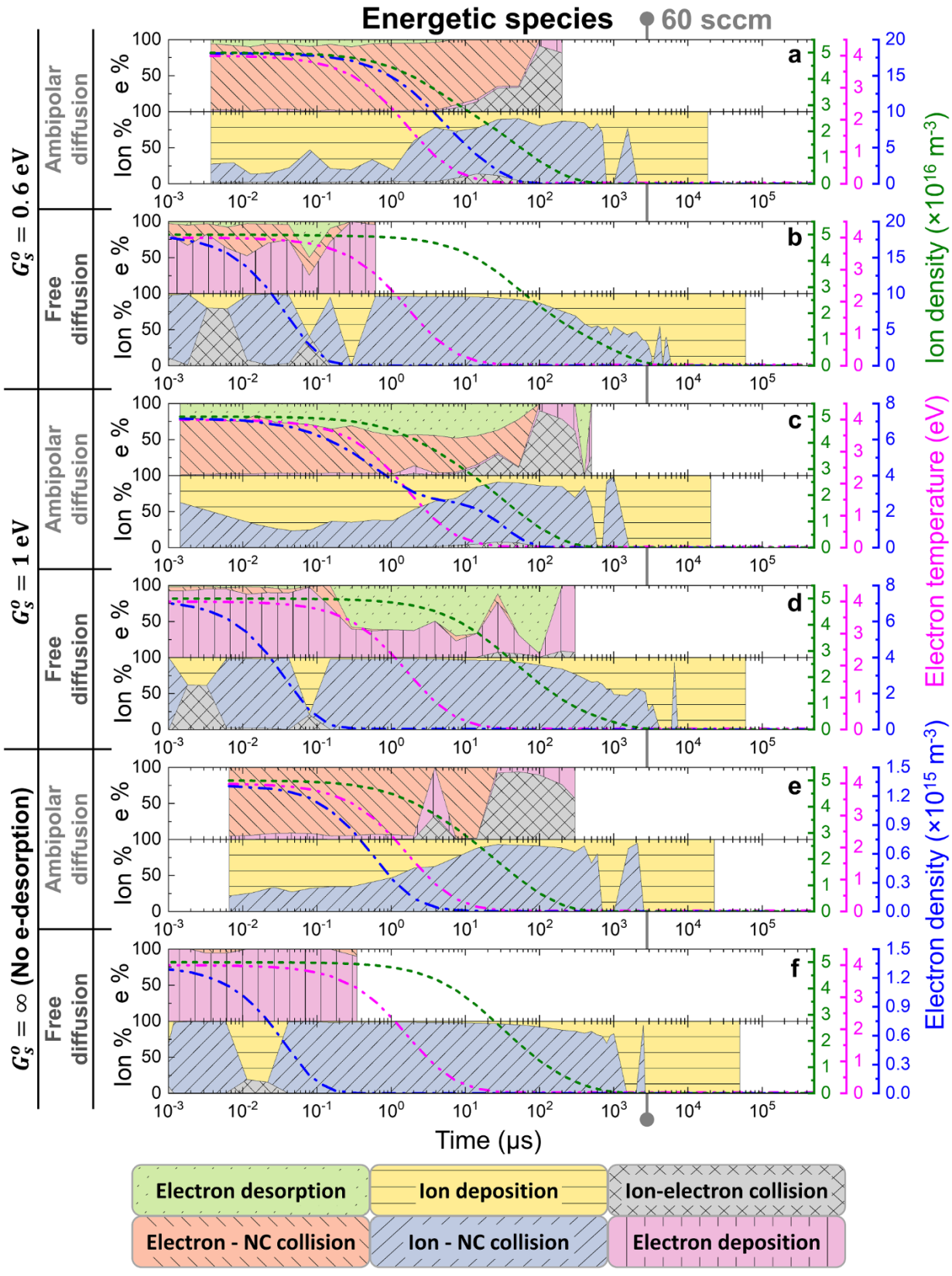

Fig. 5. Energetic species dynamics from CNMC simulation. (a-f) Area plots showing the percent occurrences of different reaction processes as a function of NC residence time in the spatial afterglow. The line plots are the changes in the electron temperature, electron density, and ion density with respect to residence time, indicated by the color of right ordinate. The CNMC simulation models and conditions are same as those utilized in Fig. 3. The grey solid line connecting plots indicates the residence time of NCs in spatial afterglow of the examined experiment [38].

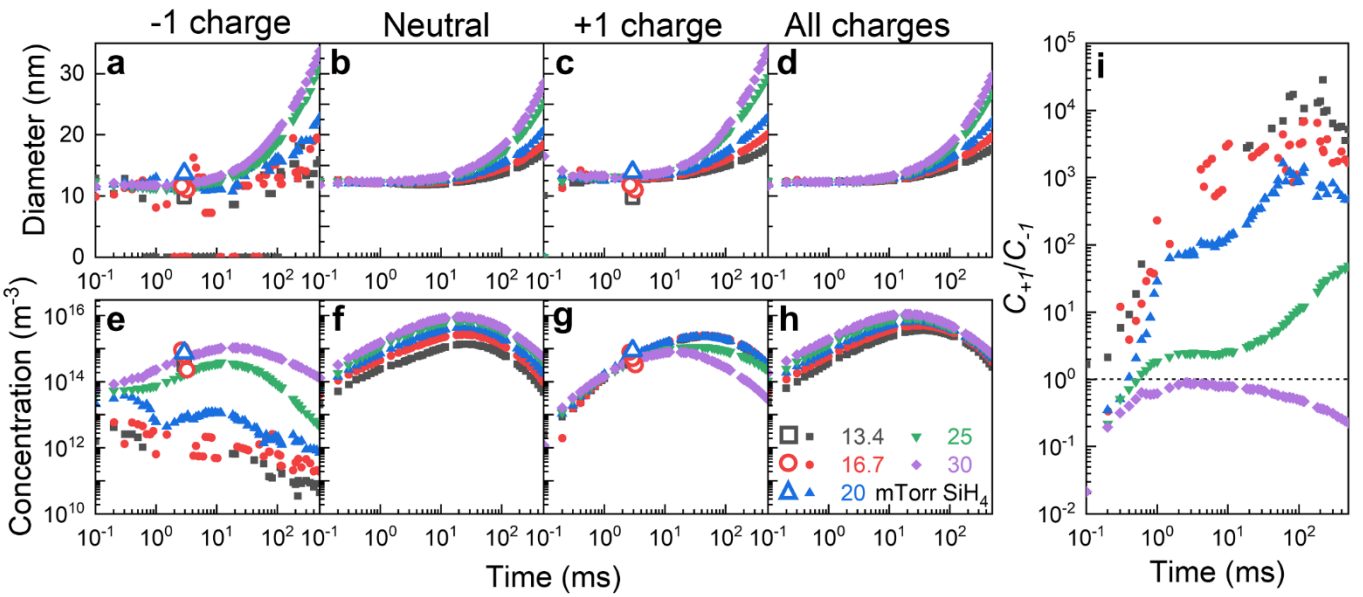

Fig. 6. The influence of precursor partial pressure on experimental and CNMC simulation results. (a-d) Mean mobility diameter of NC aggregates and (e-h) aggregate concentration of charge state (a,e) −1, (b,f) 0, (c,g) + 1 and (d,h) all charges as a function of NC residence time in spatial afterglow at various SiH_4 partial pressures. The open symbols on (a,c) are the mean diameter of NCs and on (e,g) the NC number concentration in the experiments by Chen et al [38]. (i) Concentration ratio of +1 to −1 charge state aggregates with black dotted line indicates unity to guide the eye. The simulation results were obtained with low electron solvation energy (0.6 eV) and free diffusion models implemented.

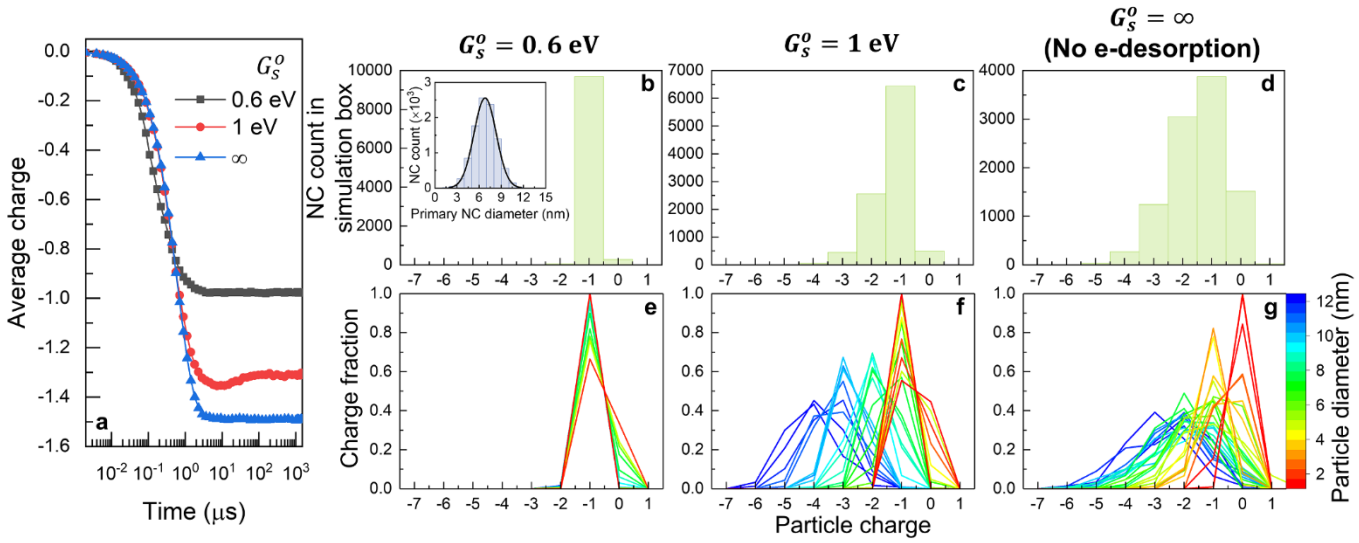

Fig. A1. Initial simulation of primary NCs in the plasma volume. (a) The average charge on NCs as a function of residence time in the plasma volume. (b-d) Primary NC charge count in the simulation box at 1.5 ms with the primary NC size distribution as an insert. (e-g) Time-averaged charge fractions of NCs from 0.1 ms onward at selected sizes in the plasma volumes, for variable electron solvation energies. (b,e) Low electron solvation energy (0.6 eV), (c,f) high electron solvation energy (1 eV), (d,g) without electron desorption. The simulations are based on conditions listed in Table 1.

CNMC simulations also show that in the narrow residence time range examined in the experiments, the aggregate size is only weakly dependent on residence time; long residence times are needed to observe substantial aggregate growth. In addition, although the aggregate concentration increases with increasing SiH_4 partial pressure for neutral and negatively charged NCs, the positively charged NC aggregate concentration decreases at elevated precursor concentrations (Fig. 6e-h). This is because the ion density is too low to reverse the NC charge state in the spatial afterglow at high precursor loading (Fig. 6i). Calculations thus suggest that extent of decharging may actually be reduced in the spatial afterglow at elevated precursor concentrations where more ions are required for neutralization, as rapid recombination and deposition of energetic species in the spatial afterglow may serve to mitigate aggregation caused by charge neutralization and charge reversal.

4. Conclusions

We develop a CNMC approach to examine NC dynamics in the unique environment of a spatial plasma afterglow, where the environment transitions from a nonthermal plasma to a gas in thermal equilibrium. The CNMC model accounts for NC collisions with electrons and ions, electron and ion wall losses, electron desorption [73] from NCs, and NC-NC collisional growth using recently developed rate expressions [54]. Models incorporating ambipolar and free diffusion of energetic

species, as well as different electron solvation energies were utilized to examine NC and NC aggregate size and charge distributions, which were compared to the ion mobility spectrometry measurements of Si NCs synthesized in a low pressure nonthermal plasma reactor [38]. This experimental study revealed clearly that many NCs are aggregates at the reactor outlet with a bipolar charge state, in contrast to the current understanding of unipolarly negative charged, monodisperse NCs in the volume of plasma reactors. The first major conclusion of the present study is that CNMC simulations demonstrate that NCs decharge in the spatial plasma afterglow region and can subsequently aggregate, with the extent of aggregation increasing with higher precursor concentration and flow residence time. While model calculations can be performed which agree quantitatively with experimentally determined mean NC aggregate sizes and concentrations, CNMC results are extremely sensitive to the model of energetic species diffusion and electron desorption employed. A second major conclusion of this study is hence that improved understanding of energetic species diffusion in spatial afterglows, charge limits and charge desorption from multiply charged particles, and likely neutral NC-charged NC rate expressions across a wide collisionality range are needed in order to more accurately model NC dynamics in afterglow environments. These phenomena are largely unique to plasma environments and existing gas phase reaction models either do not fully explain the formation of positively charged NCs, or lead to the formation of positively charged NCs and depletion of negatively charged NCs. Moreover, the developed CNMC model can be further applied to the simulation of NC charge and growth in the plasma volume, afterglow, and during transit to particle collection systems without distinguishing between plasma and spatial afterglow, provided the complete temperature profiles and ionization rate expressions are known. Therefore, in future work, a more complete NC growth depiction can be provided through CNMC, utilizing information on plasma reactor operating conditions and energy input.

Declaration of Competing Interest

The authors declare that they have no known competing financial interests or personal relationships that could have appeared to influence the work reported in this paper.

Acknowledgements

This work was primarily supported by the National Science Foundation through the University of Minnesota MRSEC under Award Number DMR-1420013. X.C. was additionally supported by Department of Energy Award DE-SC0018202. The authors acknowledge the Minnesota Supercomputing Institute (MSI) at the University of Minnesota for providing resources that contributed to the research results reported within this paper.

Appendix A. Constant number Monte Carlo simulation in the plasma volume

The simulation of NCs in a plasma to determine initial NC charge distributions is similar to the CNMC simulations described in Section 2 of the main text, but excludes NC-NC collision and NC deposition, and includes a model of NC heating as there is evidence that NCs are elevated in thermal energy above the neutral thermal energy in nonthermal plasmas [65]. Heating would influence the electron desorption rate. The inter-event time was $\Delta t_k = \frac{50}{R_T}$, where $R_T = \sum_{p=1}^{N}\left(C_{ion}\beta_{ion,p} + C_e\beta_{e,p} + R_{dsp,p}\right)$, and the selection process for events followed Eqs. (21) and (22). The electron desorption model incorporated in the plasma simulation was in accordance with spatial afterglow simulation it was applied with. If a NC collided with plasma species of same polarity, besides charge exchange, the kinetic energy of the colliding species $\frac{3}{2}k_BT$ was added to the NC internal energy; if a NC collided with the opposite polarity species, the NC was heated by ionization potential for argon of 15.76 eV [65]. All NCs were cooled through neutral gas collisions during each time step via the difference equation:

$$T_p\big|^{k+1} = T_g + \left(T_p\big|^{k} - T_g\right)\exp\left(-\frac{\frac{3}{2}k_B}{c_p m_p}\alpha_{g,p}\right) \tag{A1}$$

where c_p is NC bulk heat capacity (for silicon in this work), m_p is NC mass and $\alpha_{g,p}$ is number of neutral gas-NC collisions in a time step. Since neutral gas-NC collision rates are usually magnitudes higher than the other processes, $\alpha_{g,p}$ was generated randomly from Poisson distribution with expectation $C_g\beta_{g,p}\Delta t_k$, where C_g is gas molecule number density. The neutral gas-NC collision kernel $\beta_{g,p}$ is calculated from Eq. (B.7) with $\eta_C = \eta_{FM} = 1$. The electron density was updated at the end of each time step via Eq. (1).

Fig. A.1(a) shows the average NC charge state in the initial plasma simulation over time. We observed that NC charge distributions reached steady state near 0.1 ms. We used the NC charge distributions at 1.5 ms as the initial charge distribution in spatial afterglow simulation, which are shown in Fig. A.1(b-d). The NC residence time in the plasma volume of the experimental reactor was in the 1–3 ms range. The higher negative charge levels were observed on NCs with increasing electron solvation energy, because electron desorption effectively sets a limit of maximum excess electrons a NC can contain [57]. The time-averaged (over 10^4 time steps) charge fractions of NCs with selected diameters are shown in Fig. A.1(e-g). These results demonstrate that larger NCs can have higher levels of negative charge when the electron solvation energy is high.

Appendix B. Collision kernel models

To calculate collision kernels $\beta_{ion,p}$ and β_{ij}, we introduce the non-dimensional collision kernel H [59]:

$$H = \frac{\beta_{ij} m_{ij}\eta_C}{f_{ij}a_{ij}^3\eta_{FM}^2} \tag{B1}$$

and diffusive Knudsen number Kn_D:

$$Kn_D = \frac{\sqrt{m_{ij}k_BT}\eta_C}{f_{ij}a_{ij}\eta_{FM}} \tag{B2}$$

where β_{ij} is the collision kernel for entities i and j (e.g. ion and NC), m_{ij} and f_{ij} are reduced mass and friction coefficient of two colliding partners, respectively, a_{ij} is the sum of the radii of two collisional species, and η_C and η_{FM} are Coulombic collision enhancement factor in continuum and free molecular regime, respectively. Friction coefficients can be calculated for NCs and ions from the Stokes-Einstein equation; the friction coefficient is equivalent to the charge divided by the mobility for both ions and NCs. Considering the screen Coulomb potential, they are expressed as [54]:

$$\eta_C(\Psi_E, S_D) = \left(\int_1^{\infty} \frac{1}{r^{*2}} \exp\left(-\frac{\Psi_E}{r^*} \exp\left(-\frac{r^*}{S_D} \right) \right) dr^* \right)^{-1} \tag{B3}$$

$$\eta_{FM}(\Psi_E) = \begin{cases} 1 + \Psi_E exp\left(-\frac{1}{S_D} \right), & \Psi_E \geq 0 \\ exp\left(\Psi_E \exp\left(-\frac{1}{S_D} \right) \right), & \Psi_E \leq 0 \end{cases} \tag{B4}$$

where S_D is the non-dimensional screening length. We consider the effect of screening only for ion-NC collisions where $S_D = \frac{\lambda_D}{a_p}$ is the ratio of Debye length and NC radius. For NC-NC collisions $S_D \rightarrow \infty$ was used, though this approximation did not strongly affect the present study. Ψ_E is potential energy ratio:

$$\Psi_E = -\frac{z_i z_j e^2}{4\pi\varepsilon_0 a_{ij} k_B T} \tag{B5}$$

For ion-NC collision and NC-NC collision, the recent model by Chahl and Gopalakrishnan [54] for high potential near free molecular regime collision was implemented:

$$H = e^{\mu} H_{HS} \tag{B6}$$

where μ is a fitted function of the diffusive Knudsen number Kn_D, non-dimensional screening length S_D and potential energy ratio Ψ_E that can be found in Chahl and Gopalakrishnan [54], and H_{HS} is the hard-sphere dimensionless collision kernel, given as:

$$H_{HS} = \frac{4\pi Kn_D^2 + 25.836 Kn_D^3 + \sqrt{8\pi} Kn_D \left(11.211 Kn_D^3\right)}{1 + 3.502 Kn_D + 7.211 Kn_D^2 + 11.211 Kn_D^3} \tag{B7}$$

Appendix C. Supplementary data

Supplementary data to this article can be found online at https://doi.org/10.1016/j.cej.2020.128383.

References

[1] L. Mangolini, E. Thimsen, U. Kortshagen, High-yield plasma synthesis of luminescent silicon nanocrystals, Nano Lett. 5 (2005) 655–659.
[2] U.R. Kortshagen, R.M. Sankaran, R.N. Pereira, S.L. Girshick, J.J. Wu, E.S. Aydil, Nonthermal plasma synthesis of nanocrystals: fundamental principles, Mater., Appl., Chem. Rev. 116 (2016) 11061–11127.
[3] U. Kortshagen, Nonthermal plasma synthesis of nanocrystals: fundamentals, applications, and future research needs, Plasma Chem. Plasma Process. 36 (2016) 73–84.
[4] A. Alvarez Barragan, N.V. Ilawe, L. Zhong, B.M. Wong, L. Mangolini, A non-thermal plasma route to plasmonic TiN nanoparticles, J. Phys. Chem. C 121 (2017) 2316–2322.
[5] I. Adamovich, S.D. Baalrud, A. Bogaerts, P.J. Bruggeman, M. Cappelli, V. Colombo, U. Czarnetzki, U. Ebert, J.G. Eden, P. Favia, D.B. Graves, S. Hamaguchi, G. Hieftje, M. Hori, I.D. Kaganovich, U. Kortshagen, M.J. Kushner, N.J. Mason, S. Mazouffre, S.M. Thagard, H.R. Metelmann, A. Mizuno, E. Moreau, A.B. Murphy, B.A. Niemira, G.S. Oehrlein, Z.L. Petrovic, L.C. Pitchford, Y.K. Pu, S. Rauf, O. Sakai, S. Samukawa, S. Starikovskaia, J. Tennyson, K. Terashima, M.M. Turner, M.C. M. van de Sanden, A. Vardelle, The 2017 plasma roadmap: low temperature plasma science and technology, J. Phys. D Appl. Phys. 50 (2017), 323001.
[6] R. Körmer, M.P.M. Jank, H. Ryssel, H.-J. Schmid, W. Peukert, Aerosol synthesis of silicon nanoparticles with narrow size distribution—part 1: experimental investigations, J. Aerosol Sci. 41 (2010) 998–1007.
[7] A.A. Onischuk, A.I. Levykin, V.P. Strunin, K.K. Sabelfeld, V.N. Panfilov, Aggregate formation under homogeneous silane thermal decomposition, J. Aerosol Sci. 31 (2000) 1263–1281.
[8] T. Matsoukas, M. Russell, Particle charging in low-pressure plasmas, J. Appl. Phys. 77 (1995) 4285–4292.
[9] J.M. Luther, P.K. Jain, T. Ewers, A.P. Alivisatos, Localized surface plasmon resonances arising from free carriers in doped quantum dots, Nat. Mater. 10 (2011) 361.
[10] Z.C. Holman, C.-Y. Liu, U.R. Kortshagen, Germanium and silicon nanocrystal thin-film field-effect transistors from solution, Nano Lett. 10 (2010) 2661–2666.
[11] O.E. Semonin, J.M. Luther, S. Choi, H.-Y. Chen, J. Gao, A.J. Nozik, M.C. Beard, Peak external photocurrent quantum efficiency exceeding 100% via MEG in a quantum dot solar cell, Science 334 (2011) 1530.
[12] G.H. Carey, A.L. Abdelhady, Z. Ning, S.M. Thon, O.M. Bakr, E.H. Sargent, Colloidal quantum dot solar cells, Chem. Rev. 115 (2015) 12732–12763.
[13] G. Akay, Co-assembled supported catalysts: synthesis of nano-structured supported catalysts with hierarchic pores through combined flow and radiation induced co-assembled nano-reactors, Catalysts 6 (2016).
[14] Akay, Plasma generating—chemical looping catalyst synthesis by microwave plasma shock for nitrogen fixation from air and hydrogen production from water for agriculture and energy technologies in global warming prevention, Catalysts 10 (2020).
[15] B. Dubertret, P. Skourides, D.J. Norris, V. Noireaux, A.H. Brivanlou, A. Libchaber, In vivo imaging of quantum dots encapsulated in phospholipid micelles, Science 298 (2002) 1759.
[16] P.O. Anikeeva, J.E. Halpert, M.G. Bawendi, V. Bulović, Quantum dot light-emitting devices with electroluminescence tunable over the entire visible spectrum, Nano Lett. 9 (2009) 2532–2536.
[17] D. Jurbergs, E. Rogojina, L. Mangolini, U. Kortshagen, Silicon nanocrystals with ensemble quantum yields exceeding 60%, Appl. Phys. Lett. 88 (2006), 233116.
[18] R. Gresback, N.J. Kramer, Y.i. Ding, T. Chen, U.R. Kortshagen, T. Nozaki, Controlled doping of silicon nanocrystals investigated by solution-processed field effect transistors, ACS Nano 8 (2014) 5650–5656.
[19] K.-Y. Cheng, R. Anthony, U.R. Kortshagen, R.J. Holmes, High-efficiency silicon nanocrystal light-emitting devices, Nano Lett. 11 (2011) 1952–1956.
[20] C.-Y. Liu, Z.C. Holman, U.R. Kortshagen, Hybrid solar cells from P3HT and silicon nanocrystals, Nano Lett. 9 (2009) 449–452.
[21] S. Zhou, Y. Ding, X. Pi, T. Nozaki, Doped silicon nanocrystals from organic dopant precursor by a SiCl4-based high frequency nonthermal plasma, Appl. Phys. Lett. 105 (2014), 183110.
[22] Z.C. Holman, U.R. Kortshagen, A flexible method for depositing dense nanocrystal thin films: impaction of germanium nanocrystals, Nanotechnology 21 (2010) 335302.
[23] P. Firth, Z.C. Holman, Aerosol impaction-driven assembly system for the production of uniform nanoparticle thin films with independently tunable thickness and porosity, ACS Appl. Nano Mater. 1 (2018) 4351–4357.

[24] E. Thimsen, M. Johnson, X. Zhang, A.J. Wagner, K.A. Mkhoyan, U.R. Kortshagen, E.S. Aydil, High electron mobility in thin films formed via supersonic impact deposition of nanocrystals synthesized in nonthermal plasmas, Nat. Commun. 5 (2014) 5822.

[25] B.L. Greenberg, Z.L. Robinson, Y. Ayino, J.T. Held, T.A. Peterson, K.A. Mkhoyan, V. S. Pribiag, E.S. Aydil, U.R. Kortshagen, Metal-insulator transition in a semiconductor nanocrystal network, Sci. Adv. 5 (2019) eaaw1462.

[26] N.P. Rao, H.J. Lee, M. Kelkar, D.J. Hansen, J.V.R. Heberlein, P.H. McMurry, S. L. Girshick, Nanostructured materials production by hypersonic plasma particle deposition, Nanostruct. Mater. 9 (1997) 129–132.

[27] K.E. Mackie, A.C. Pebley, M.M. Butala, J. Zhang, G.D. Stucky, M.J. Gordon, Microplasmas for direct, substrate-independent deposition of nanostructured metal oxides, Appl. Phys. Lett. 109 (2016), 033110.

[28] R.J. Anthony, K.-Y. Cheng, Z.C. Holman, R.J. Holmes, U.R. Kortshagen, An all-gas-phase approach for the fabrication of silicon nanocrystal light-emitting devices, Nano Lett. 12 (2012) 2822–2825.

[29] N.B. Uner, E. Thimsen, Nonequilibrium plasma aerotaxy of size controlled GaN nanocrystals, J. Phys. D Appl. Phys. 53 (2019), 095201.

[30] S. Ghosh, X. Chen, C. Li, B.A. Olson, C.J. Hogan, Fragmentation and film growth in supersonic nanoaggregate aerosol deposition, AIChE J. (2020) e16874.

[31] L. Mädler, A.A. Lall, S.K. Friedlander, One-step aerosol synthesis of nanoparticle agglomerate films: simulation of film porosity and thickness, Nanotechnology 17 (2006) 4783–4795.

[32] J. Lee, C.J. Hogan, Computational predictions of porosities, pore size distributions, and conductivities of aerosol deposited particulate films, Powder Technol. 378 (Part A) (2021) 400–409.

[33] K.D. Benkstein, N. Kopidakis, J. van de Lagemaat, A.J. Frank, Influence of the percolation network geometry on electron transport in dye-sensitized titanium dioxide solar cells, J. Phys. Chem. B 107 (31) (2003) 7759–7767.

[34] L. Mangolini, Monitoring non-thermal plasma processes for nanoparticle synthesis, J. Phys. D Appl. Phys. 50 (2017), 373003.

[35] B. van Minderhout, T. Peijnenburg, P. Blom, J.M. Vogels, G.M.W. Kroesen, J. Beckers, The charge of micro-particles in a low pressure spatial plasma afterglow, J. Phys. D Appl. Phys. 52 (2019) 32LT03.

[36] X. Chen, T. Seto, U.R. Kortshagen, C.J. Hogan, Determination of nanoparticle collision cross section distribution functions in low pressure plasma synthesis reactors via ion mobility spectrometry, Nano Futures 3 (2019), 015002.

[37] G. Sharma, N. Abuyazid, S. Dhawan, S. Kshirsagar, R.M. Sankaran, P. Biswas, Characterization of particle charging in low-temperature, atmospheric-pressure, flow-through plasmas, J. Phys. D Appl. Phys. 53 (2020), 245204.

[38] X. Chen, T. Seto, U.R. Kortshagen, C.J. Hogan, Size and structural characterization of Si nanocrystal aggregates from a low pressure nonthermal plasma reactor, Powder Technol. 373 (2020) 164–173.

[39] X. Chen, S. Ghosh, D.T. Buckley, R.M. Sankaran, C.J. Hogan, Characterization of the state of nanoparticle aggregation in non-equilibrium plasma synthesis systems, J. Phys. D Appl. Phys. 51 (2018), 335203.

[40] A. Boje, J. Akroyd, S. Sutcliffe, J. Edwards, M. Kraft, Detailed population balance modelling of TiO2 synthesis in an industrial reactor, Chem. Eng. Sci. 164 (2017) 219–231.

[41] C.S. Lindberg, M.Y. Manuputty, P. Buerger, J. Akroyd, M. Kraft, Numerical simulation and parametric sensitivity study of titanium dioxide particles synthesised in a stagnation flame, J. Aerosol Sci. 138 (2019), 105451.

[42] D. Hou, D. Zong, C.S. Lindberg, M. Kraft, X. You, On the coagulation efficiency of carbonaceous nanoparticles, J. Aerosol Sci. 140 (2020), 105478.

[43] B. Zhao, Z. Yang, M.V. Johnston, H. Wang, A.S. Wexler, M. Balthasar, M. Kraft, Measurement and numerical simulation of soot particle size distribution functions in a laminar premixed ethylene-oxygen-argon flame, Combust. Flame 133 (2003) 173–188.

[44] M.E. Mueller, H. Pitsch, Large eddy simulation of soot evolution in an aircraft combustor, Phys. Fluids 25 (2013), 110812.

[45] S.A. Davari, D. Mukherjee, Kinetic Monte Carlo simulation for homogeneous nucleation of metal nanoparticles during vapor phase synthesis, AIChE J. 64 (2018) 18–28.

[46] L. Ravi, S.L. Girshick, Coagulation of nanoparticles in a plasma, Phys. Rev. E 79 (2009), 026408.

[47] R. Le Picard, A.H. Markosyan, D.H. Porter, S.L. Girshick, M.J. Kushner, Synthesis of silicon nanoparticles in nonthermal capacitively-coupled flowing plasmas: processes and transport, Plasma Chem. Plasma Process. 36 (2016) 941–972.

[48] P. Agarwal, S.L. Girshick, Numerical modeling of an RF argon-silane plasma with dust particle nucleation and growth, Plasma Chem. Plasma Process. 34 (2014) 489–503.

[49] M. Smith, T. Matsoukas, Constant-number Monte Carlo simulation of population balances, Chem. Eng. Sci. 53 (1998) 1777–1786.

[50] F.E. Kruis, A. Maisels, H. Fissan, Direct simulation Monte Carlo method for particle coagulation and aggregation, AIChE J. 46 (2000) 1735–1742.

[51] B.A. Thomson, J.V. Iribarne, Field induced ion evaporation from liquid surfaces at atmospheric pressure, J. Chem. Phys. 71 (1979) 4451–4463.

[52] M. Labowsky, J.B. Fenn, J. Fernandez de la Mora, A continuum model for ion evaporation from a drop: effect of curvature and charge on ion solvation energy, Anal. Chim. Acta 406 (2000) 105–118.

[53] F.X. Bronold, H. Deutsch, H. Fehske, Physisorption kinetics of electrons at plasma boundaries, Eur. Phys. J. D 54 (2009) 519–544.

[54] H.S. Chahl, R. Gopalakrishnan, High potential, near free molecular regime Coulombic collisions in aerosols and dusty plasmas, Aerosol Sci. Technol. 53 (2019) 933–957.

[55] H. Shin, W. Zhu, D.J. Economou, V.M. Donnelly, Ion energy distributions, electron temperatures, and electron densities in Ar, Kr, and Xe pulsed discharges, J. Vacuum Sci. Technol. A 30 (2012), 031304.

[56] L. Couedel, A.A. Samarian, M. Mikikian, L. Boufendi, Influence of the ambipolar-to-free diffusion transition on dust particle charge in a complex plasma afterglow, Phys. Plasmas 15 (2008), 063705.

[57] M. Gamero-Castano, J.F.d.l. Mora, Kinetics of small ion evaporation from the charge and mass distribution of multiply charged clusters in electrosprays, J. Mass Spectrom. 35 (2000) 790–803.

[58] C.J. Hogan Jr, J. Fernández de la Mora, Tandem ion mobility-mass spectrometry (IMS-MS) study of ion evaporation from ionic liquid-acetonitrile nanodrops, PCCP 11 (2009) 8079–8090.

[59] R. Gopalakrishnan, C.J. Hogan, Coulomb-influenced collisions in aerosols and dusty plasmas, Phys. Rev. E 85 (2012), 026410.

[60] A. Maisels, F. Jordan, F. Einar Kruis, H. Fissan, A study of nanoparticle aerosol charging by Monte Carlo simulations, J. Nanopart. Res. 5 (2003) 225–235.

[61] A. Maisels, F.E. Kruis, H. Fissan, Coagulation in bipolar aerosol chargers, J. Aerosol Sci. 35 (2004) 1333–1345.

[62] J. Wei, F.E. Kruis, GPU-accelerated Monte Carlo simulation of particle coagulation based on the inverse method, J. Comput. Phys. 249 (2013) 67–79.

[63] S. Khalili, Y. Lin, A. Armaou, T. Matsoukas, Constant number Monte Carlo simulation of population balances with multiple growth mechanisms, AIChE J. 56 (2010) 3137–3145.

[64] Y. Lin, K. Lee, T. Matsoukas, Solution of the population balance equation using constant-number Monte Carlo, Chem. Eng. Sci. 57 (2002) 2241–2252.

[65] L. Mangolini, U. Kortshagen, Selective nanoparticle heating: another form of nonequilibrium in dusty plasmas, Phys. Rev. E 79 (2009).

[66] L. Li, H.S. Chahl, R. Gopalakrishnan, Comparison of the predictions of Langevin Dynamics-based diffusion charging collision kernel models with canonical experiments, J. Aerosol Sci. 140 (2020), 105481.

[67] L.i. Li, R. Gopalakrishnan, An experimentally validated model of diffusion charging of arbitrary shaped aerosol particles, J. Aerosol Sci. 151 (2021) 105678.

[68] T. Tamadate, H. Higashi, T. Seto, C.J. Hogan, Calculation of the ion–ion recombination rate coefficient via a hybrid continuum-molecular dynamics approach, J. Chem. Phys. 152 (2020), 094306.

[69] J.E. Allen, Probe theory - the orbital motion approach, Phys. Scr. 45 (1992) 497–503.

[70] H.M. Mott-Smith, I. Langmuir, The theory of collectors in gaseous discharges, Phys. Rev. 28 (1926) 727–763.

[71] R. Le Picard, S.L. Girshick, The effect of single-particle charge limits on charge distributions in dusty plasmas, J. Phys. D Appl. Phys. 49 (2016), 095201.

[72] M.S. Veshchunov, On the saturation of unipolar and bipolar diffusion charging of aerosols, Aerosol Sci. Technol. 55 (2021) 1–10.

[73] A. Woodard, K. Shojaei, C. Berrospe-Rodriguez, G. Nava, L. Mangolini, Electron emission from particles strongly affects the electron energy distribution in dusty plasmas, J. Vac. Sci. Technol., A 38 (2020), 023005.

[74] M. Gamero-Castaño, J. Fernández de la Mora, Mechanisms of electrospray ionization of singly and multiply charged salt clusters, Anal. Chim. Acta 406 (2000) 67–91.

[75] F.P. Incropera, D.P. Dewitt;, T.L. Bergman;, A.S. Lavine, Fundamentals of heat and mass transfer, 6th ed.2007.

[76] Z. Sun, R. Axelbaum, J. Huertas, Monte Carlo simulation of multicomponent aerosols undergoing simultaneous coagulation and condensation, Aerosol Sci. Technol. 38 (2004) 963–971.

[77] Y.P. Raizer, Gas Discharge Physics, first ed., Springer-Verlag, Berlin Heidelberg, 1991.

[78] R.N. Varney, Drift velocities of ions in krypton and xenon, Phys. Rev. 88 (1952) 362–364.

[79] M.A. Lieberman, S. Ashida, Global models of pulse-power-modulated high-density, low-pressure discharges, Plasma Sources Sci. Technol. 5 (1996) 145–158.

[80] C.S. Wang, S.K. Friedlander, The self-preserving particle size distribution for coagulation by Brownian motion: II. Small particle slip correction and simultaneous shear flow, J. Colloid Interf. Sci. 24 (1967) 170–179.

[81] C. Larriba, C.J. Hogan, M. Attoui, R. Borrajo, J.F. Garcia, J.F. de la Mora, The mobility-volume relationship below 3.0 nm examined by tandem mobility-mass measurement, Aerosol Sci. Technol. 45 (2011) 453–467.

[82] C. Zhang, T. Thajudeen, C. Larriba, T.E. Schwartzentruber, C.J. Hogan, Determination of the scalar friction factor for nonspherical particles and aggregates across the entire Knudsen number range by direct simulation Monte Carlo, Aerosol Sci. Technol. 46 (2012) 1065–1078.

[83] C. Larriba, C.J. Hogan, Ion mobilities in diatomic gases: measurement versus prediction with non-specular scattering models, J. Phys. Chem. A 117 (2013) 3887–3901.

[84] C. Larriba-Andaluz, F. Carbone, The size-mobility relationship of ions, aerosols, and other charged particle matter, J. Aerosol Sci. 151 (2021), 105659.

[85] Y.S. Cheng, H.C. Yeh, Theory of a screen-type diffusion battery, J. Aerosol Sci. 11 (1980) 313–320.

[86] S.L. Girshick, Particle nucleation and growth in dusty plasmas: on the importance of charged-neutral interactions, J. Vac. Sci. Technol., A 38 (2020) 011001.

[87] B. Santos, L. Cacot, C. Boucher, F. Vidal, Electrostatic enhancement factor for the coagulation of silicon nanoparticles in low-temperature plasmas, Plasma Sources Sci. Technol. 28 (2019), 045002.